Optical Materials 86 (2018) 71–78

Contents lists available at ScienceDirect

Optical Materials

journal homepage: www.elsevier.com/locate/optmat

# $Zn_{1-x}Mg_xO$ nanoparticles prepared by the polymeric precursor method: Correlation between photoluminescence and local structure

Rodrigo Cury de Oliveira[a], Denis Expedito Martins[a], Maria Inês Basso Bernardi[b], Alexandre Mesquita[a,*]

[a] Universidade Estadual Paulista (Unesp), Instituto de Geociências e Ciências Exatas, Departamento de Física, Rio Claro, SP, Brazil
[b] Universidade de São Paulo, Instituto de Física de São Carlos, São Carlos, SP, Brazil

ARTICLE INFO

*Keywords:*
ZnO
Z1-xMgxO
Photoluminescence
Polymeric precursor method
XANES
EXAFS
FTIR
FE-SEM

ABSTRACT

ZnO is an n-type semiconductor having a wide band gap which has been studied as green phosphors because of its luminescence properties, although the centers and mechanisms responsible for its luminescence are still a matter of controversy. Band gap engineering of ZnO can be achieved by the incorporation of Mg atoms, resulting in the modification of the deep level emission in the visible region. In this study, nanostructured $Zn_{1-x}Mg_xO$ samples were prepared through the polymeric precursor method and their structural and photoluminescent properties were characterized. FE-SEM images reveal a polygonal morphology of ZnO nanoparticles and a uniform particle size ranging from 35 to for 91 nm depending on the annealing temperature. XRD results show that $Zn_{1-x}Mg_xO$ samples crystallized completely without the presence of secondary phases (up to 20 at. %) and the diffraction patterns correspond to the hexagonal wurtzite structure with $P6_3mc$ space. Theoretical and experimental XANES spectra at Zn K-edge along FTIR measurements suggest occurrence of O vacancies. These vacancies are related to the green emission of photoluminescence spectra for ZnO samples, which is centered at ~529 nm. As the Mg content increases, an enhancement of this emission is observed, which is associated with the recombination of electrons in Mg interstitials donor states and holes at Zn vacancies.

## 1. Introduction

Nanocrystalline semiconductors have intermediate electronic properties between those of molecular structure and macrocrystalline solid, presenting a wide range of applications [1–4]. These materials attracted attention not only by new properties and its possible potential technological applications, but also the search for a better understanding of the physical and chemical processes that cause these new properties [1]. Among these materials, zinc oxide (ZnO) is an n-type semiconductor having a wide band gap of approximately 3.3 eV which has been utilized as green phosphors because of its excellent luminescence properties under high-energy excitations [5–7]. Wide-gap oxide semiconductors are attractive materials as phosphors if they could exhibit visible emissions arising from defect levels created in the band gap [5]. However, defect-related emissions are usually sensitive to synthetic conditions and suffer from reproducibility [5].

Although ZnO luminescence has been the subject of studies for several decades, the centers and mechanisms responsible for many of its luminescence properties are still a matter of controversy [2,3,5,7–11]. To explain the green emission, various models have been proposed, including the involvement of several lattice defects, such as O vacancies ($V_O$), O interstitials ($O_i$), antisite O ($O_{Zn}$), Zn antisite ($Zn_O$), Zn vacancies ($V_{Zn}$) and Zn interstitials ($Zn_i$) [2,3,5,7–12]. Indeed, green emissions in different samples can have different origins despite similar position and width, which means the origin of the defect emission cannot be postulated simply by noting the similarities with previously published spectra for ZnO prepared by other fabrication methods [13]. Among different experiment methods to probe the structure of ZnO nanoparticles, X-ray absorption spectroscopy (XAS) can be a useful technique to probe these defects. In fact, XAS technique is a powerful tool for the investigation of local structures and provides meaningful additional structural information on materials [14]. Although the local structural data afforded by XAS are usually not sufficient to construct a whole structural model, they often provide valuable information about the local structural peculiarities [15]. These characteristics are useful to interpret photoluminescent properties.

Novel properties in ZnO nanostructures can be reached by altering the structural parameters through doping, which can tune the energy band gap from ultraviolet to visible wavelengths depending on the nature of the doping and its concentration [8,9,16]. Several elements

* Corresponding author.adress:
*E-mail address:* mesquita@rc.unesp.br (A. Mesquita).

https://doi.org/10.1016/j.optmat.2018.09.044
Received 23 May 2018; Accepted 27 September 2018
Available online 02 October 2018
0925-3467/ © 2018 Elsevier B.V. All rights reserved.

have been used to dope ZnO, such as Cd, Co, Fe, Er, Mg and Mn [16–18]. Among these elements, Mg has gained attention because of the increase of the band gap and the modification of the deep level emission of ZnO in the visible region, which has made possible interesting applications such as UV detector, light emitting diodes and solar cells [6,9,12]. Moreover, an alloy of ZnO and MgO is easily expected because the similarity between ionic radius of $Mg^{2+}$ (0.57 Å) and $Zn^{2+}$ (0.60 Å) [8]. It has been reported that this kind of substitution causes an enhancement of the green emission, although there is no consensus about its origin. Trunk et al. reported that the green emission peak for $Zn_{1-x}Mg_xO$ (ZnO:Mg) films was ascribed to the free-to-bound type transitions between $Zn_i$ and $V_{Zn}$ [19], whereas Li et al. assigned to the oxygen vacancies or impurity for thin films and single-crystal microprisms [20,21]. Hammad et al. suggested that the green emission peak for ZnO:Mg hollow spheres was attributed to the transition between $V_O$ or $O_{Zn}$ and donor-acceptor pair [22]. Fang et al. reported that the green emission peak is attributed to the oxygen vacancies or donor-acceptor pair generated by Mg incorporation on Zn sites [12].

Currently, there are many methods available to synthesize ZnO:Mg nanomaterial, including pulsed laser deposition, two-step method, molecular-beam epitaxy, chemical vapor deposition, spray pyrolysis, sputtering, electrospinning, sol-gel and hydrothermal synthesis [5,8,10,20,23,24]. Among these methods, the sol-gel route has been successfully used to prepare nanostructured materials because of its low cost, lower temperatures of synthesis and stoichiometric control. The polymeric precursor method, also referred as modified Pechini method, is a type of sol-gel route based on the chelation of metal cations with an α-hydroxycarboxylic acid, such as citric acid, to form stable metal complexes; then polymerize with a polyhydroxy alcohol, such as ethylene glycol, forming a polymeric resin which is pyrolyzed [25,26]. Several advantages are associated with this method, such as low toxicity, compositional homogeneity, doping at molecular level in solution and reduced segregation of metal ions [25–29]. This method has been shown to be an effective procedure to prepare doped or pure nanoparticles of ZnO [27–29]. However, as far as we are aware, there is a lack of studies on the nature of lattice defects in this kind of material prepared by the polymeric precursor method and their influence on photoluminescence properties.

In the study presented here, nanostructured $Zn_{1-x}Mg_xO$ samples were prepared by the polymeric precursor method. The short- and long-range structure of these samples was characterized by X-ray diffraction (XRD), field emission scanning electron microscopy (FE-SEM), XAS at Zn K-edge, Fourier transform infrared spectroscopy (FTIR) and correlated to photoluminescence (PL) properties.

## 2. Experimental procedure

$Zn_{1-x}Mg_xO$ samples were prepared by the polymeric precursor method (details of this method can be found elsewhere [25,26,30]) with x = 0.00 (ZnO), x = 0.10 (ZM10), x = 0.20 (ZM20), x = 0.30 (ZM30) and x = 0.40 (ZM40). This method is illustrated in the scheme of Fig. 1. Zinc nitrate hexahydrate, $Zn(NO_3)_2{\cdot}6H_2O$ (98%, Aldrich), magnesium nitrate, $Mg(NO_3)_2$ (98%, Vetec), ethylene glycol, $C_2H_6O_2$ (99.5%, Synth) and citric acid, $C_6H_8O_7$ (99.5%, Synth) were used as raw materials in stoichiometric quantities. Zinc and magnesium citrate were formed by the dissolution of $Zn(NO_3)_2{\cdot}6H_2O$ and $Mg(NO_3)_2$ in a citric acid aqueous solution under constant stirring. The citrate solution was stirred at 70 °C to obtain a clear homogeneous solution. After the cation homogenization in the solutions, $C_2H_6O_2$ was added to promote a polyesterification reaction. The citric acid/ethylene glycol mass ratio was fixed at 60/40. As the preparation involves the polymeric network formation, the samples were heated at 400 °C for 4 h in order to eliminate the organic precursors. After this heat treatment, ZnO samples were annealed at 500, 600 and 700 °C for 2 h and ZnO:Mg samples were annealed at 700 °C for 2 h. Mg-undoped samples were labeled as ZnO_*x*, where *x* represents the annealing temperature in Celsius degrees.

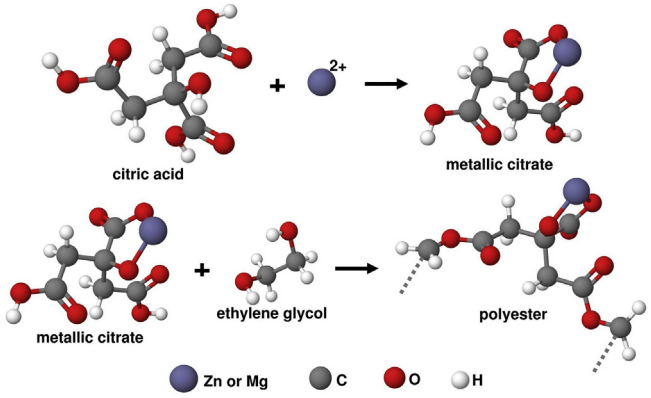


**Fig. 1.** Scheme illustrating the polymeric precursor method.

The XRD measurements were performed at room temperature on a RigakuUltima 4 powder diffractometer with geometry θ-2θ, a rotating anode X-ray source (Cu-$K_\alpha$ radiation, λ = 1.542 Å) and a scintillation detector. The data were collected with a step size of 0.02° and the count time was 5 s per step. The microstructural characterization was carried out in a high resolution scanning electron microscope Zeiss Sigma operating at 3 kV. The grain size distribution was determined for each sample and then fitted using a log-normal distribution function. Ti K-edge X-ray absorption spectra (9659 eV) were collected at the LNLS (National Synchrotron Light Laboratory, Brazil) facility using the D04B-XAS1 beamline. The LNLS storage ring was operated at 1.36 GeV and 100–160 mA. The spectra were collected in transmission mode using a Si(111) channel-cut monochromator at room temperature. The sample thicknesses were optimized by the Multi-Platform Applications for XAFS (MAX) software package Absorbix code [31]. Normalized XANES (X-ray absorption near edge structure) spectra were extracted with the MAX-Cherokee code. The theoretical XANES spectra were calculated by the FEFF9 *ab initio* code [32,33] whose input files were issued from MAX-Crystalffrev software, which takes into account substitution disorder and random vacancies in the structure [31]. EXAFS (extended X-ray absorption fine structure) spectra were extracted with the MAX-Cherokee code while the fitting procedure and comparison between experimental and theoretical EXAFS curves were conducted with the MAX-Roundmidnight package. The theoretical EXAFS spectra were calculated by the FEFF9 *ab initio* code [32,33] whose input files were issued from MAX-Crystalffrev software. In our work the relevant measure of the fit quality, the reduced statistical $\chi^2$ is named QF (quality factor). FTIR measurements were performed using a spectrometer Thermo Scientific Nicolet IS10. Photoluminescence spectra were collected at room temperature with a Thermal Jarrel-Ash Monospecmonochromator and a Hamamatsu R446 photomultiplier. The 350.6 nm exciting wavelength of a krypton ion laser (Coherent Innova) was used; the output of the laser was maintained at 200 mW.

## 3. Results and discussion

In order to check the morphology of the ZnO matrix prepared by the precursor polymeric method, FE-SEM measurements were performed. Fig. 2 shows the FE-SEM images for ZnO powders annealed at 500 (ZnO_500), 600 (ZnO_600) and 700 °C (ZnO_700). The images in this figure reveal an irregular morphology of ZnO nanoparticles and a uniform particle size for each annealing temperature. The particle size distribution was evaluated and the results obtained for the set of samples are presented in Fig. 2(d). The average particle size for ZnO_500, ZnO_600 and ZnO_700 are 35 ± 1, 58 ± 1 and 91 ± 2 nm, respectively, with a quasi-linear growth rate as a function of the annealing temperature. This result confirms that the polymeric precursor method can be an effective procedure for the preparation of ZnO nanostructured samples.

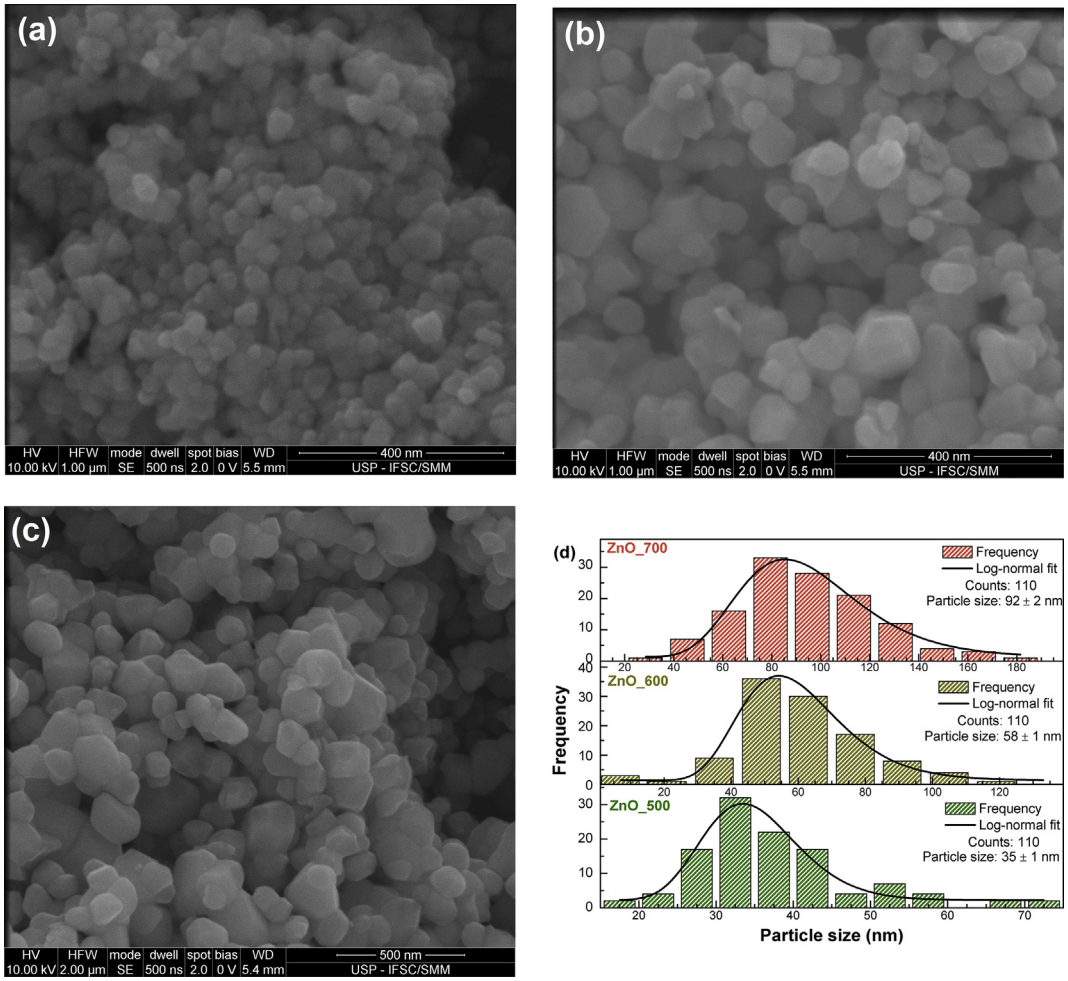


**Fig. 2.** FE-SEM images for (a) ZnO_500, (b) ZnO_600 and (c) ZnO_700 nanostructured samples. The (c) particle size distribution is also presented.

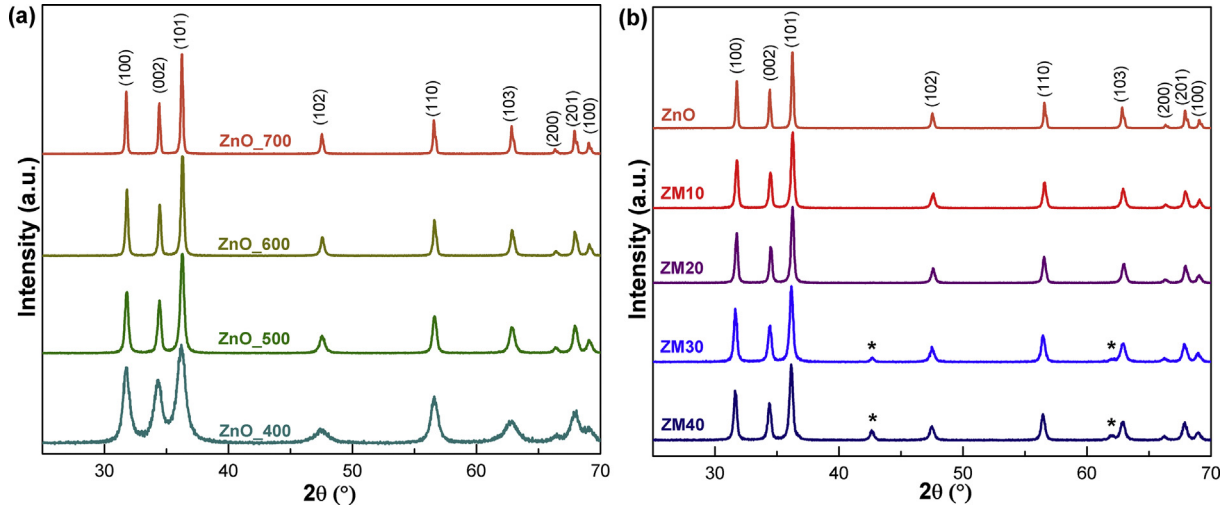


**Fig. 3.** XRD patterns of ZnO samples as a function of (a) annealing temperature and (b) Mg content.

Fig. 3 shows the XRD patterns collected at room temperature as a function of the annealing temperature (3(a)) and the amount of magnesium (3(b)). ZnO samples crystallized completely without the presence of secondary phases even for samples only with the pyrolysis at 400 °C. As the annealing temperature increases, the full width at half maximum of the peaks decreases, indicating a growth of crystallite size, in good agreement with FE-SEM images. According to the literature, the diffraction planes of ZnO samples annealed at all temperatures correspond to those expected for polycrystalline wurtzite ZnO with space group $P6_3mc$ [18]. As can be seen in Fig. 3(b), XRD patterns for ZM10 e ZM20 do not exhibit secondary phases, indicating that the Mg ions in these samples are taking the place of Zn in the ZnO wurtzite structure. On the other hand, secondary phase is observed for ZM30 and ZM40 samples. The spurious diffraction peaks are labeled with asterisk in

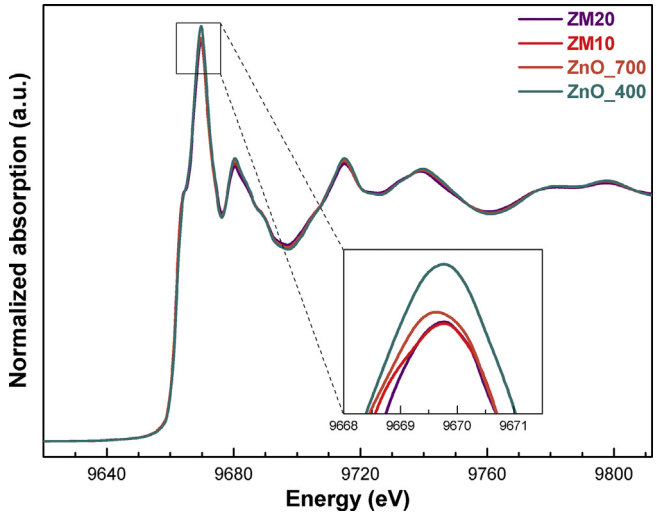


**Fig. 4.** Normalized experimental XANES spectra of ZnO:Mg samples. The lower-right inset shows details of white line of these spectra.

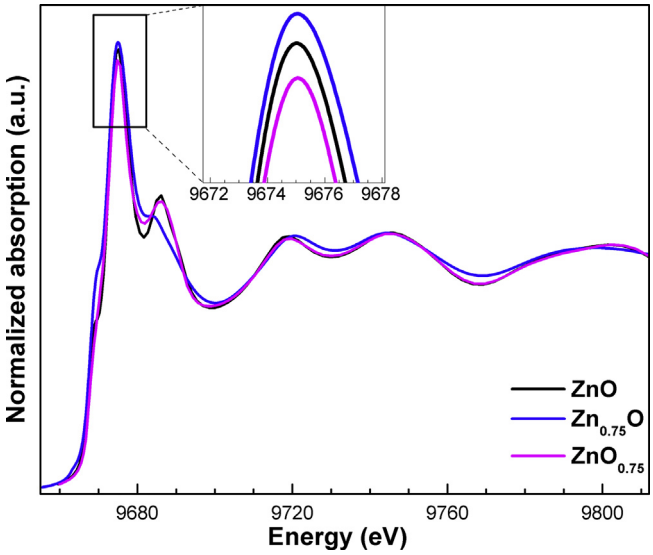


**Fig. 5.** Calculated XANES spectra for ZnO, $Zn_{0.75}O$ and $ZnO_{0.75}$ compositions.

Fig. 3(b) and are related with the formation of MgO phase, which is an indication that the solubility limit is less than 30 at. % of Mg.

The structure of ZnO:Mg samples was also characterized by XAS measurements. XANES spectra give information on the coordination symmetry and the valence of ions incorporated in a solid. The energy of the absorption edge shifts according to the valence of the absorbing ion, since the binding energy of bound electrons rises as the valence increases. Also, the shape of the absorption edge depends on the unfilled local density of states and the coordination symmetry of the absorbing element. The spectrum at the Zn *K*-edge is characteristic of the electron transition from the 1s state to empty 4*p* states.

In Fig. 4 normalized XANES spectra at Zn *K*-edge is shown for the ZnO_400, ZnO_700, ZM10 and ZM20 samples. These spectra exhibit similar *K*-edge white line shapes and XANES features to those previously reported for tetrahedral coordinated ZnO [17,34]. The lower-right inset of Fig. 4 presents the evolution of the intensity of the peak related to the white line maximum for the set of samples. As the annealing temperature increases, the intensity of the white line peak increases, whereas no changes in intensity in this peak are observed as the Mg ions are incorporated to ZnO matrix. In order to comprehend this behavior, calculated XANES spectrum for ZnO compound using *ab initio* FEFF code [32,33] was obtained. This spectrum (black line) is shown in Fig. 5 and, as can be seen, reproduces satisfactorily the experimental spectra. The input files for FEFF code with cluster radius of 6.0 Å were generated using CRYSTALFFREV software [31] and our XRD measurements. Calculated XANES spectra were also obtained varying the occupation rates of Zn and O sites in the ZnO matrix. In Fig. 5, the spectra labeled as $Zn_{0.75}O$ and $ZnO_{0.75}$ represent the calculated XANES spectra with occupation rates of 0.75 at the Zn or O site, respectively.

As can be seen in the lower-right inset, the intensity of white line increased as the occupation rate at the Zn site decreased for the calculated spectra. This increase in the calculated spectra can be related to the fact that the K-edge XANES here reproduces the density distribution of the unoccupied *p*-like states around Zn atoms. Reduction of the Zn atomic content causes an increased localization of the Zn *p*-like states and, in consequence, sharper resonances [35]. On the other hand, the decrease in the occupation rate at the O site in the XANES calculations resulted in a white line peak with lower intensity, in agreement with the observed behavior for our set of samples. Thus, the calculated XANES spectra indicate that the decreases in the intensity of the white line peak for the nanostructured ZnO samples with the increase of annealing temperature (upper-left inset in Fig. 5) can be associated with the decrease of the occupation rate at the O site. In other words, the changes in the region of the white line can be attributed to the formation of oxygen vacancy sites as a result of the annealing. Even more, these results also suggest that the oxygen vacancies are formed close to the Zn ions.

The short-range structural data provided by extended X-ray absorption fine structure (EXAFS) offers an element-specific insight, giving quantitative information about the number, position and identity of atoms surrounding the absorbing element as well as structural disorder within the coordination spheres. In order to obtain quantitative information of the local structure around Zn atoms, Fourier transform curves were then back Fourier transformed between 1.0 and 5.0 Å to obtain the experimental EXAFS spectra to fit using a theoretical model calculated from FEFF9 code and crystallographic information according to the XRD measurements.

The fitted $k\chi(k)$ and $k^3$ weighted Fourier transforms of the nanostructured ZM samples are shown in Fig. 6(a) and (b), respectively. In all fits, we considered single scattering paths corresponding to the first (four O atoms), second (6 Zn atoms), third (6 Zn atoms) and fourth (10 O atoms) shells around Zn absorber atom according to the hexagonal wurtzite structure with $P6_3mc$ space group. The number of free parameters was kept smaller than the number of independent points, which is defined as $N_{ind} = 2\Delta R\Delta k/\pi$, where $\Delta R$ is the width of the *R*-space filter windows and $\Delta k$ is the actual interval of the fit in the *k*-space [36]. The reliability of the fit, determined by a quality factor (QF) [36], coordination number (N), interatomic distances (R) and Debye-Waller factor ($\sigma^2$) relative to the fits are shown in Table 1.

According to the structural model, the first intense peak, between 1.0 and 2.0 Å in the Fourier transforms corresponds to single scattering interaction between the first O atoms around the absorber atom. The single scattering interactions relative to Zn—Zn and Zn—O (beyond the first O neighbors) paths correspond to the peaks and shoulders observed between 2.0 and 3.5 Å. This region also includes multiple scattering paths such as Zn—*O*—O, Zn—*O*—Zn—O, Zn—*O*—O—O and Zn—Zn—O interactions. As can be viewed in Table 1, the obtained QF factors indicate the reliability of the fits, which is confirmed by the comparison of the fitted (lines) and experimental (symbols) data at Fig. 6(a) and (b). No changes within the uncertainty are observed in the distance between each shell and Zn absorber atom. In the same way, Debye-Waller factor values do not exhibit alterations within the uncertainty.

In order to comprehend the formation of oxygen vacancies pointed out by XAS measurements, FTIR measurements were performed in the wavenumber range between 4000 and 500 $cm^{-1}$ for ZnO samples as a function of annealing temperature. These FTIR spectra are shown in Fig. 7 in which nine features can be identified. In this Fig., feature

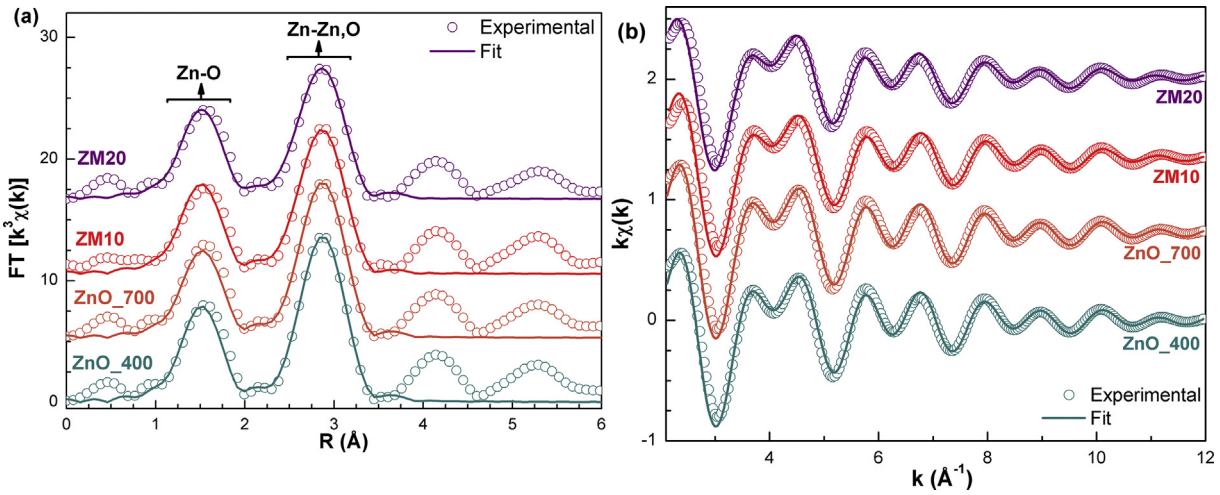


**Fig. 6.** Fitted and experimental (a) $k^3$−weighted Fourier transforms and (b) $k\chi(k)$ spectra for ZnO:Mg samples.

**Table 1**
Zn K-edge EXAFS simulation results. R is the distance from the absorber atom, N is the average coordination number, $\sigma^2$ the Debye-Waller factor and QF the quality factor.

| Sample | Shell | R (A) | N | σ2 (Å$^2$) | QF |
|---|---|---|---|---|---|
| ZnO_400 | Zn-$O_I$ | 1.96(1) | 4.7(6) | 0.0052(13) | 8.68 |
| | Zn−$Zn_I$ | 3.3(1) | 6.2(1.5) | | |
| | Zn−$Zn_{II}$ | 3.2(1) | 6.1(1.4) | 0.0081(4) | |
| | Zn−$O_{II}$ | 3.7(4) | 6.9(2.9) | | |
| ZnO_700 | Zn-$O_I$ | 1.96(1) | 4.8(6) | 0.0058(15) | 6.72 |
| | Zn−$Zn_I$ | 3.27(2) | 6.2(1.2) | 0.008(1) | |
| | Zn−$Zn_{II}$ | 3.21(2) | 6.0(1.0) | | |
| | Zn−$O_{II}$ | 3.72(3) | 7.5(3.2) | | |
| ZM10 | Zn-$O_I$ | 1.95(2) | 4.7(1) | 0.0058(31) | 6.77 |
| | Zn−$Zn_I$ | 3.27(2) | 6.2(1.1) | 0.0080(7) | |
| | Zn−$Zn_{II}$ | 3.2(1) | 5.8(9) | | |
| | Zn−$O_{II}$ | 3.7(1) | 5.1(2.9) | | |
| ZM20 | Zn-$O_I$ | 1.96(1) | 4.7(7) | 0.0058(37) | 5.63 |
| | Zn−$Zn_I$ | 3.3(1) | 6.2(1.1) | 0.0081(7) | |
| | Zn−$Zn_{II}$ | 3.2(1) | 5.7(1.0) | | |
| | Zn−$O_{II}$ | 3.71(6) | 3.3(2.8) | | |

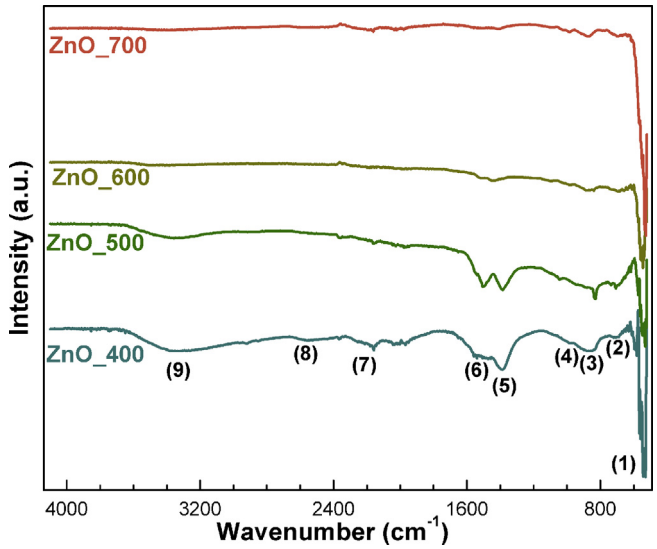


**Fig. 7.** FTIR spectra for ZnO samples as a function of annealing temperature.

labeled as (1) corresponds to stretching mode of Zn−O [27,37,38], feature labeled as (2) corresponds to scissoring mode of $COO^-$ group [39], features labeled as (3) and (4) correspond to C−OH [27], features labeled as (5) and (8) correspond to stretching vibration of C−H [27,40], feature labeled as (6) corresponds to asymmetric and symmetric C=O stretching modes [37,38], feature labeled as (7) corresponds to C=C vibrations [40] and feature labeled as (9) corresponds to OH-group stretching vibrations [27,37,38,40]. As can be seen in Fig. 7, all these bands are clearly observed up to the annealing temperature of 500 °C. From 600 °C, only feature (1) does not show changes whereas the other bands are suppressed, indicating that the residual polymeric resin is eliminated from this annealing temperature.

In the preparation of ZnO through the polymeric precursor method, citric acid was used to coordinate $Zn^{2+}$, forming −Zn−OOC−C(OH)−COOH complexes. The COOH groups in these complexes also react with ethylene glycol (cross-linking agents that contain a large amount of $-CH_2$ and −OH groups), finally forming polymer resin networks such as −Zn−OOC−C−COOC-$(CH_2)_n$-COO−Zn− [41]. In the subsequent pyrolysis process, most organic species decompose into $H_2O$ and $CO_2$ which are eliminated from the system, but a small amount of them can decompose to create interstitial carbon defects or substitutional carbon defects for the Zn atom. These organic species are linked to the Zn−*O*−Zn networks, such as Zn−*O*−C−C-R, −Zn−*O*−C−*O*−Zn−, etc. The bond energies of Zn−O, C−O and C−C are approximately 159, 1077 and 610 kJ/mol, respectively [42]. Thus, it is noted that the Zn−O bond energy is lower than that of the C−O and C−C bonds and the bond energies lead to a significant dependence on the order of bond cleavage on chemical and thermal environment [41]. Therefore, with subsequent heat treatment, the initial cleavage occurs at the Zn−O bonds, which modifies the intermolecular chemical environment and removes a portion of the oxygen from the network along with the carbon. The disruption of the above bond occurs at a temperature where the healing of the fragmented bonds and the normalization of the coordination state are thermodynamically forbidden [41]. Thus, the increase in the annealing temperature would cause an increase in the number of oxygen vacancies, explaining the results of XAS analysis.

Fig. 8(a) presents the photoluminescence (PL) spectra for ZnO samples measured at room temperature. As can be seen in this Fig., the spectra are highly asymmetrical, broadened and centered at green region, with multiple peaks indicating the involvement of different luminescence centers in the radiative processes. It is also evident from this Fig. that the intensity of PL spectra mainly in the green region (500–550 nm) increases as the annealing temperature increases. As shown by the FE-SEM characterization, the ZnO samples show an increase in particle size as a function of the annealing temperature. The

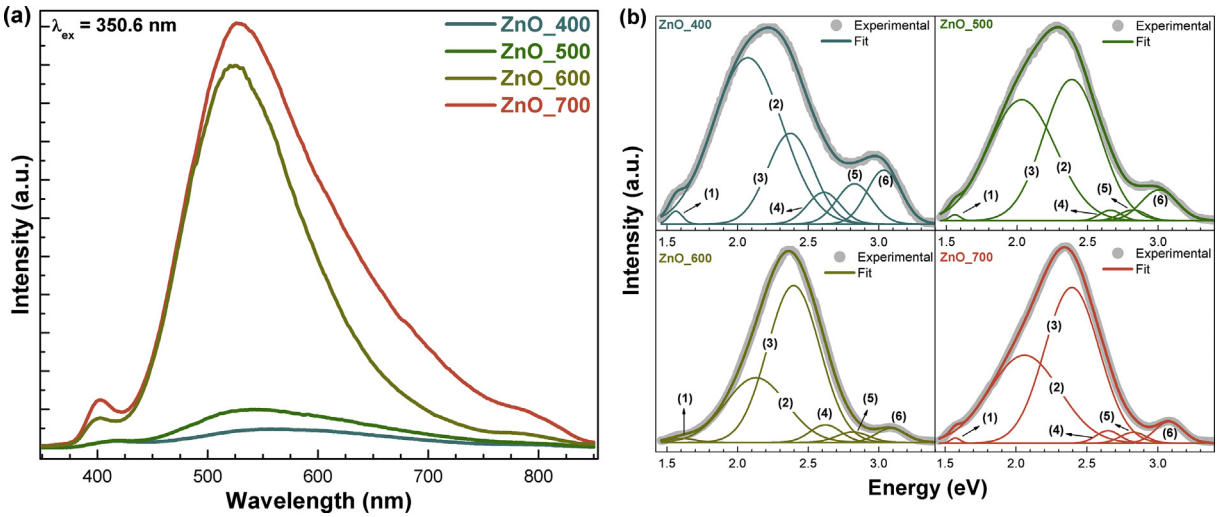


**Fig. 8.** (a) PL spectra measured at room temperature for ZnO samples as a function of annealing temperature and (b) deconvoluted PL spectra for ZnO samples as a function of energy.

relationship between the increase in PL intensity and particle size has been observed in the literature and attributed to an increase in the electron-phonon coupling due to the Fröhlich interaction [43–45]. However, it does not seem to be our case since the PL intensity increases substantially with annealing temperature of 600 °C and does not follow the quasi-linear growth rate of particle size as observed in FE-SEM measurements.

To investigate the several noticeable emissions in Fig. 8(a), the PL spectra of ZnO samples were deconvoluted, whose fitted curves are shown in Fig. 8(b) as a function of the energy. All PL spectra were appropriately fitted taking into account six peaks and no substantial red or blue shifts are observed with annealing temperature. The peak labeled as (1) in near-infrared region (1.56–1.59 eV) presents a dependence of the intensity with the annealing temperature. Near-infrared emission in ZnO has been explained by the donor-acceptor transition between $V_O$ and $V_{Zn}$ and/or the radiative recombination of shallowly trapped electrons with deeply trapped holes at $O_i$ [46]. Because of the intensity dependence with annealing temperature and the appearance of $V_O$ indicated by XAS and FTIR measurements, we believe that the first hypothesis is more reasonable.

The peaks labeled as (2) and (3) in red-orange and green regions (2.07–2.12 eV and 2.37–2.39 eV, respectively) show a strong dependence of intensity with the annealing temperature, mainly the peak (3). It has been reported that the enhancement of this green emission corresponds to the local level composed by oxide antisite defect rather than $V_O$, $V_{Zn}$, $Zn_i$ or $O_i$ [11]. Nonetheless, oxygen antisites have higher formation energies and, therefore, are not expected to play a role in ZnO under near-equilibrium conditions [6]. According to Trunk et al. [19], the red-orange emission can be understood assuming that the radiative transitions involve electrons trapped at a $V_O$ donor level at 2 eV above the valence band. This assumption is consistent, but the green emission seems also to be originated in defects caused by $V_O$ since the intensity dependence of this emission with annealing temperature as well as the appearance of $V_O$ indicated by our results. According to Kayaci et al. [47], $V_O^{++}$, $V_O^{+}$ and $V_O$ are donor type defects and the $V_O^{+}$ state can capture an electron from conduction band and forms a neutral state ($V_O$), from which a transition to valence band occurs by the emission of green light. Furthermore, $V_O^{+}$ can capture a hole from valence band and forms a $V_O^{++}$ state into which an electron recombines from conduction band and emits at a higher wavelength. Thus, peaks labeled as (2) and (3) are related to defects originated by $V_O^{++}$ and $V_O$ states, respectively.

Blue emissions in PL spectra of ZnO has been associated with zinc lattice defects in which their origin are due to two probable transitions related to $V_{Zn}$ deep level and $Zn_i$ shallow level, *i.e.* an electron from conduction band recombines with the hole at $V_{Zn}$ or an electron is captured by $Zn_i$ then recombines with the hole in the valence band [19,47,48]. Thus, considering the ascribed origin of the above mentioned near-infrared and green emissions and an energy band gap of ~3.3 eV [6,11,19,47,48], it is consistent to deduce that the peak labeled as (4) (2.61–2.66 eV) is related to the transition of an electron from conduction band to a deep level hole at $V_{Zn}$. Concerning the peak labeled as (5) (2.81–2.82eV), this emission can be attributed to the recombination of an electron at $Zn_i$ with a hole in the valence band since this energy is in agreement with previous calculation of this energy level for ZnO matrix [11,48]. Finally, the peak labeled as (6) in UV region (3.01–3.08 eV) has been ascribed to near band-edge emission, in which an electron from the free exciton level recombines with a hole in the valence band [6,11,19,47,48].

Fig. 9 presents the PL spectrum measured at room temperature for ZnO:Mg samples. In this Fig., the PL spectrum of ZnO_700 is also shown and the upper-right inset exhibits the deconvoluted PL spectrum as a function of the energy for ZM20 sample. This spectrum exhibits similar

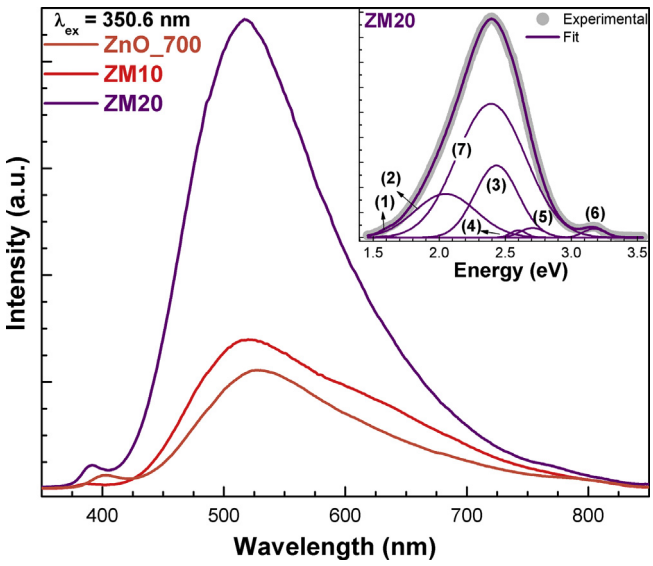


**Fig. 9.** PL spectra measured at room temperature for ZnO:Mg samples. The upper-right inset shows deconvoluted PL spectra for ZM20 sample as a function of energy.

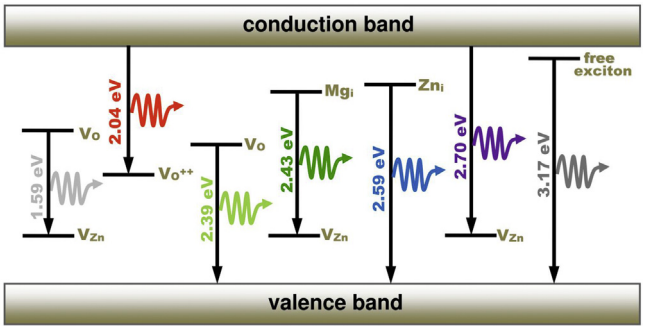


**Fig. 10.** Schematic diagram of the various emissions corresponding to PL spectrum for ZM20 sample.

features compared to that one reported by Li et al. [2], although reports from different groups have shown PL spectra of Mg-doped ZnO centered at lower wavelengths [3,5,8–10]. As can be seen in Fig. 9, the PL spectrum is centered in green region and the intensity increases remarkably as Mg atoms are incorporated to ZnO matrix. Because of this increase in green region, the deconvolution was performed considering an additional peak in relation to the six ones in PL spectra of ZnO samples. The peak labeled as (6), which is attributed to the excitonic recombination corresponding to the near band-edge emission of ZnO band-gap [2,9], shifts to higher energies with Mg content. It is known that Mg-doped ZnO materials exhibit blue-shifted emissions arising from recombination of excitons under influence of the band-gap broadening [5,19].

Concerning the peak labeled as (7), Mallika et al. assigned this emission to a shallow donor, and the nature of the shallow donor might be the complex defect of $Zn_i$ [3]. This statement is supported in their work by the fact that this emission does not change with Mg concentration. However, this is not the case in our samples. Additionally, according to Qiu et al. [49], there are two primary forms of Mg occupations: lattice substitution and interstitial occupations. From the phase diagram of ZnO—MgO binary systems, the thermodynamic solubility limit of Mg ions in the ZnO lattice would be about 4% [49], although our XRD measurements and several papers indicate a considerably higher value [3,12,19,50–52]. When the Mg content is less than solubility limit, the majority of Mg ions are likely substituted in the Zn sites of ZnO, while when more Mg ions were dissolved in the ZnO lattice, an excess of Mg ions might enter into the interstitial sites ($Mg_i$). Therefore, the interstitial doping model along with the substitution model of the lattice site should be taken into account for the generation of the green emission for ZnO:Mg samples. According to Trunk et al. [19], this emission is interpreted in terms of a competing supply of electrons from slightly deeper $Mg_i$ donor states, which recombines with holes at $V_{Zn}$. Moreover, the peak labeled as (3) and associated with a transition from $V_O$ to valence band does not exhibits changes with Mg incorporation, which would be expected since this substitution is homovalent and consequently there is no formation of $V_O$. Furthermore, Boonchun et al. has calculated the band gap position of the $V_O$ states in ZnO:Mg for Mg concentrations up to 20% and concluded that Mg incorporation might have very little effect on the $V_O$ level [19,53]. A schematic diagram of the various emissions corresponding to PL spectrum for ZM20 sample is shown in Fig. 10.

## 4. Conclusions

In this study, nanostructured $Zn_{1-x}Mg_xO$ samples were prepared through the polymeric precursor method and their structural and photoluminescent properties were characterized. FE-SEM images reveal a polygonal morphology of ZnO nanoparticles and a uniform particle size ranging from 35 to for 92 nm depending on the annealing temperature. XRD results show that $Zn_{1-x}Mg_xO$ samples crystallized completely without the presence of secondary phases (up to 20 at. %) and the diffraction patterns correspond to the hexagonal wurtzite structure with $P6_3mc$ space. Theoretical and experimental XANES spectra at Zn K-edge along FTIR measurements suggest occurrence of O vacancies. These vacancies are related to the green emission of photoluminescence spectra for ZnO samples, which is centered at ~529 nm. As the Mg content increases, an enhancement of this emission is observed, which is associated with the recombination of electrons in Mg interstitials donor states and holes at Zn vacancies.

## Acknowledgements

The authors thank FAPESP (through project 2013/12993-4), CNPq and Capes funding agencies. The research was partially carried out at LNLS National Laboratory of Synchrotron Light (proposal number XAFS1-17750), Brazil.

## References

[1] V.I. Klimov, S.A. Ivanov, J. Nanda, M. Achermann, I. Bezel, J.A. McGuire, A. Piryatinski, Single-exciton optical gain in semiconductor nanocrystals, Nature 447 (2007) 441–446.
[2] J.L. Li, H.Z. Zhuang, J. Wang, P. Xu, Synthesis, characterization, and optical properties of Mg-doped zinc oxide single-crystal microprisms, Phys. Status Solidi 208 (2011) 136–139.
[3] A.N. Mallika, A.R. Reddy, K.S. Babu, C. Sujatha, K.V. Reddy, Structural and photoluminescence properties of Mg substituted ZnO nanoparticles, Opt. Mater. 36 (2014) 879–884.
[4] P.B. Taunk, R. Das, D.P. Bisen, R.K. Tamrakar, Structural characterization and photoluminescence properties of zinc oxide nano particles synthesized by chemical route method, J. Radiat. Res. Appl. Sci. 8 (2015) 433–438.
[5] Y. Ogawa, S. Fujihara, Blue luminescence of MgZnO and CdZnO films deposited at low temperatures, J. Electrochem. Soc. 154 (2007) J283–J288.
[6] A. Janotti, C.G. Van de Walle, Fundamentals of zinc oxide as a semiconductor, Rep. Prog. Phys. 72 (2009) 126501.
[7] K. Vanheusden, C.H. Seager, W.L. Warren, D.R. Tallant, J.A. Voigt, Correlation between photoluminescence and oxygen vacancies in ZnO phosphors, Appl. Phys. Lett. 68 (1996) 403–405.
[8] J.W. Kim, H.S. Kang, J.H. Kim, S.Y. Lee, J.K. Lee, M. Nastasi, Variation of structural, electrical, and optical properties of Zn1-xMgxO thin films, J. Appl. Phys. 100 (2006) 033701.
[9] R. Udayabhaskar, B. Karthikeyan, Enhanced fluorescence and local vibrational mode in near-white-light-emitting ZnO:Mg nanorods system, J. Am. Ceram. Soc. 98 (2015) 1807–1811.
[10] S.S. Cetin, I. Uslu, A. Aytimur, S. Ozcelik, Characterization of Mg doped ZnO nanocrystallites prepared via electrospinning, Ceram. Int. 38 (2012) 4201–4208.
[11] B.X. Lin, Z.X. Fu, Y.B. Jia, Green luminescent center in undoped zinc oxide films deposited on silicon substrates, Appl. Phys. Lett. 79 (2001) 943–945.
[12] D.Y. Fang, C.L. Li, N. Wang, P. Li, P. Yao, Structural and optical properties of Mg-doped ZnO thin films prepared by a modified Pechini method, Cryst. Res. Technol. 48 (2013) 265–272.
[13] K.H. Tam, C.K. Cheung, Y.H. Leung, A.B. Djurisic, C.C. Ling, C.D. Beling, S. Fung, W.M. Kwok, W.K. Chan, D.L. Phillips, L. Ding, W.K. Ge, Defects in ZnO nanorods prepared by a hydrothermal method, J. Phys. Chem. B 110 (2006) 20865–20871.
[14] V.A. Shuvaeva, I. Pirog, Y. Azuma, K. Yagi, K. Sakaue, H. Terauchi, I.P. Raevskii, K. Zhuchkov, M.Y. Antipin, The local structure of mixed-ion perovskites, J. Phys. Condens. Matter 15 (2003) 2413–2421.
[15] V.A. Shuvaeva, D. Zekria, A.M. Glazer, Q. Jiang, S.M. Weber, P. Bhattacharya, P.A. Thomas, Local structure of the lead-free relaxor ferroelectric (KxNa1-x)(0.5) Bi0.5TiO3, Phys. Rev. B 71 (2005) 174114.
[16] S.A. Azzez, Z. Hassan, J.J. Hassan, M.S. Mukhlif, M.S. Mandi, M. Bououdina, Effect of temperature on hydrothermally grown high-quality single-crystals Mg-doped ZnO nanorods for light-emitting diode application, J. Lumin. 192 (2017) 634–643.
[17] V.M. de Almeida, A. Mesquita, A.O. de Zevallos, N.C. Mamani, P.P. Neves, X. Gratens, V.A. Chitta, W.B. Ferraz, A.C. Doriguetto, A.C.S. Sabioni, H.B. de Carvalho, Room temperature ferromagnetism promoted by defects at zinc sites in Mn-doped ZnO, J. Alloy. Comp. 655 (2016) 406–414.
[18] A. Mesquita, F.P. Rhodes, R.T. da Silva, P.P. Neves, A.O. de Zevallos, M.R.B. Andreeta, M.M. de Lima, A. Cantarero, I.S. da Silva, M.A. Boselli, X. Gratens, V.A. Chitta, A.C. Doriguetto, W.B. Ferraz, A.C.S. Sabioni, H.B. de Carvalho, Dynamics of the incorporation of Co into the wurtzite ZnO matrix and its magnetic properties, J. Alloy. Comp. 637 (2015) 407–417.
[19] M. Trunk, V. Venkatachalapathy, A. Galeckas, A.Y. Kuznetsov, Deep level related photoluminescence in ZnMgO, Appl. Phys. Lett. 97 (2010) 211901.
[20] H. Li, Y.Z. Zhang, X.J. Pan, T. Wang, E.Q. Xie, The effects of thermal annealing on properties of MgxZn1-xO films by sputtering, J. Alloy. Comp. 472 (2009) 208–210.
[21] J.L. Li, H.Z. Zhuang, J. Wang, P. Xu, Synthesis, characterization, and optical properties of Mg-doped zinc oxide single-crystal microprisms, Phys. Status Solidi 208 (2011) 136–139.
[22] T.M. Hammad, J.K. Salem, Synthesis and characterization of Mg-doped ZnO hollow

spheres, J. Nanoparticle Res. 13 (2011) 2205–2212.
[23] M. Rouchdi, E. Salmani, B. Fares, N. Hassanain, A. Mzerd, Synthesis and characteristics of Mg doped ZnO thin films: experimental and ab-initio study, Results Phys. 7 (2017) 620–627.
[24] N. Guo, X.Q. Wei, R.R. Zhao, X.J. Xu, Preparation and optical properties of Mg-doped ZnO nanorods, Appl. Surf. Sci. 317 (2014) 400–404.
[25] M.P. Pechini, Method of Preparing Lead and Alkaline - Earth Titanates and Niobates and Coatings Method Using the Same to Form a Capacitor in: U. S. Patent, 1967.
[26] M. Kakihana, "Sol-Gel" preparation of high temperature superconducting oxides, J. Sol. Gel Sci. Technol. 6 (1996) 7–55.
[27] N. Rana, S. Chand, A.K. Gathania, Band gap engineering of ZnO by doping with Mg, Phys. Scripta 90 (2015) 085502.
[28] K.T.G. Carvalho, S.C. Fidelis, O.F. Lopes, C. Ribeiro, Effect of processing variables on the photocatalytic properties of ZnO thin films prepared using the polymeric precursor method, Ceram. Int. 41 (2015) 10587–10594.
[29] N. Rana, S. Chand, A.K. Gathania, Tailoring the structural and optical properties of ZnO by doping with Cd, Ceram. Int. 41 (2015) 12032–12037.
[30] A. Mesquita, M.I. Basso Bernardi, C. Godart, P.S. Pizani, A. Michalowicz, V.R. Mastelaro, Grain size effect on the structural and dielectric properties of Pb0.85La0.15TiO3 ferroelectric ceramic compound, Ceram. Int. 38 (2012) 5879–5887.
[31] A. Michalowicz, J. Moscovici, D. Muller-Bouvet, K. Provost, MAX: multiplatform applications for XAFS, J. Phys. Conf. 190 (2009) 012034.
[32] J.J. Rehr, J.J. Kas, F.D. Vila, M.P. Prange, K. Jorissen, Parameter-free calculations of x-ray spectra with FEFF9, Phys. Chem. Chem. Phys. 12 (2010) 5503–5513.
[33] A.L. Ankudinov, B. Ravel, S.D. Conradson, J.J. Rehr, Real-space multiple-scattering calculation and interpretation of x-ray-absorption near-edge structure, Phys. Rev. B 58 (1998) 7565.
[34] F. Decremps, F. Datchi, A.M. Saitta, A. Polian, S. Pascarelli, A. Di Cicco, J.P. Itie, F. Baudelet, Local structure of condensed zinc oxide, Phys. Rev. B 68 (2003).
[35] A.L. Curcio, M.I.B. Bernardi, A. Mesquita, Local structure and photoluminescence properties of nanostructured Zn1-xMnxS material, Phys. Status Solidi C 12 (2015) 1367–1371.
[36] S.S. Hasnain, Report on the International Workshops on Standards and Criteria in XAFS. In X-ray Absorption Fine Structure: Proceedings of the VI International Conference on X-ray Absorption Fine Structures, Ellis Horwood, New York, 1991.
[37] C.A. Amorim, G. Gozzi, D.L. Chinaglia, F.J. dos Santos, L.F. Santos, Synthesis of transparent semiconducting metal-oxides via polymeric precursor route for application in thin-film field-effect transistors, MRS Adv. 1 (2016) 489–494.
[38] S. Maensiri, P. Laokul, V. Promarak, Synthesis and optical properties of nanocrystalline ZnO powders by a simple method using zinc acetate dihydrate and poly (vinyl pyrrolidone), J. Cryst. Growth 289 (2006) 102–106.
[39] M.A. Verges, A. Mifsud, C.J. Serna, Formation of rod-like zinc-oxide microcrystals in homogeneous solutions, J. Chem. Soc. Faraday. Trans. 86 (1990) 959–963.
[40] S.T. Lu, H.H. Wang, J. Zhou, X.H. Wu, W. Qin, Atomic layer deposition of ZnO on carbon black as nanostructured anode materials for high-performance lithium-ion batteries, Nanoscale 9 (2017) 1184–1192.
[41] C.K. Lin, C.M. Zhang, J. Lin, Phase transformation and photoluminescence properties of nanocrystalline ZrO2 powders prepared via the Pechini-type sol-gel process, J. Phys. Chem. C 111 (2007) 3300–3307.
[42] D.R. Lide, CRC Handbook of Chemistry and Physics, 84th ed., CRC Press, Boca Raton, 2004.
[43] U. Choppali, E. Kougianos, S.P. Mohanty, B.P. Gorman, Polymeric precursor derived nanocrystalline ZnO thin films using EDTA as chelating agent, Sol. Energy Mater. Sol. Cell. 94 (2010) 2351–2357.
[44] W.T. Hsu, K.F. Lin, W.F. Hsieh, Reducing exciton-longitudinal-optical phonon interaction with shrinking ZnO quantum dots, Appl. Phys. Lett. 91 (2007) 181913.
[45] H.M. Cheng, K.F. Lin, H.C. Hsu, W.F. Hsieh, Size dependence of photoluminescence and resonant Raman scattering from ZnO quantum dots, Appl. Phys. Lett. 88 (2006) 261909.
[46] M.S. Wang, Y.J. Zhou, Y.P. Zhang, E.J. Kim, S.H. Hahn, S.G. Seong, Near-infrared photoluminescence from ZnO, Appl. Phys. Lett. 100 (2012) 101906.
[47] F. Kayaci, S. Vempati, I. Donmez, N. Biyikli, T. Uyar, Role of zinc interstitials and oxygen vacancies of ZnO in photocatalysis: a bottom-up approach to control defect density, Nanoscale 6 (2014) 10224–10234.
[48] H.B. Zeng, G.T. Duan, Y. Li, S.K. Yang, X.X. Xu, W.P. Cai, Blue luminescence of ZnO nanoparticles based on non-equilibrium processes: defect origins and emission controls, Adv. Funct. Mater. 20 (2010) 561–572.
[49] X.Q. Qiu, L.P. Li, J. Zheng, J.J. Liu, X.F. Sun, G.S. Li, Origin of the enhanced photocatalytic activities of semiconductors: a case study of ZnO doped with Mg2+, J. Phys. Chem. C 112 (2008) 12242–12248.
[50] A. Ohtomo, M. Kawasaki, T. Koida, K. Masubuchi, H. Koinuma, Y. Sakurai, Y. Yoshida, T. Yasuda, Y. Segawa, MgxZn1-xO as a II-VI widegap semiconductor alloy, Appl. Phys. Lett. 72 (1998) 2466–2468.
[51] W.L. Guan, J. Lian, Y.X. Yu, Z.Z. Sun, M.L. Zhao, X. Wang, W.F. Zhang, Optical properties of MgxZn1-xO thin films deposited on silicon and sapphire substrate by rf magnetron sputtering, Optik 125 (2014) 5167–5170.
[52] H.T. Shi, C.F. Alfaro, K.R. Barrera, T.L. Hessong, S.R. Halbert, Influence of Mg-doping on the optical properties of ZnO thin films prepared via electrochemical deposition, Phys. Status Solidi 210 (2013) 1163–1170.
[53] A. Boonchun, W.R.L. Lambrecht, First-principles study of oxygen vacancies in MgxZn1-xO alloys, Phys. Rev. B 81 (2010) 024103.